

# Assessing the Roles of Three Eddy Types in Restratifying the Labrador Sea after Deep Convection

RENSKE GELDERLOOS\*, CAROLINE A. KATSMAN AND SYBREN S. DRIJFHOUT

*Royal Netherlands Meteorological Institute, De Bilt, Netherlands*

---

\* *Corresponding author address:* Renske Gelderloos, KNMI, Global Climate Division, P.O. Box 201, 3730

AE De Bilt, Netherlands.

E-mail: [renske.gelderloos@knmi.nl](mailto:renske.gelderloos@knmi.nl)

## ABSTRACT

5    Restratification after deep convection is one of the key factors in determining the temporal  
variability of dense water formation in the Labrador Sea. In the subsurface it is primarily  
governed by lateral buoyancy fluxes during early spring. The roles of three different eddy  
types in this process are assessed using an idealized model of the Labrador Sea that simulates  
the restratification season. The first eddy type, warm-core Irminger Rings, is shed from the  
10   boundary current along the west coast of Greenland. All along the coastline the boundary  
current forms Boundary Current Eddies. The third type, Convective Eddies, arises directly  
around the convection area. In the model, the latter two eddy types are together responsible  
for replenishing 30% of the winter heat loss within six months. Irminger Rings add another  
45% to this number. Our results thus confirm that the presence of Irminger Rings is essential  
15   for a realistic amount of restratification in this area. The model results are compared to  
observations using theoretical estimates of restratification time scales derived for the three  
eddy types. The time scales are also used to explain contradicting conclusions in previous  
studies on their respective roles.

# 1. Introduction

20 Labrador Sea Water (LSW) is one of the main mode waters in the North Atlantic Ocean (Lazier 1973; Lazier et al. 2002). It is formed in winter by deep convection (Clarke and Gascard 1983; LabSeaGroup 1998), facilitated by the harsh climatic conditions in this region and the regional ocean circulation (Marshall and Schott 1999). It spreads southwards and eastwards into the North Atlantic Ocean and beyond, where it partly sets the density structure  
25 at intermediate depths (Bower et al. 2009). As such it also contributes to the variability in the global meridional overturning circulation (Eden and Willebrand 2001; Yashayaev 2007; Biastoch et al. 2008).

Besides wintertime atmospheric conditions, one of the key processes that determine the interannual and interdecadal variability of LSW formation (Dickson et al. 1996; Lazier et al.  
30 2002; Kieke et al. 2007; Yashayaev 2007) is restratification after deep convection<sup>1</sup>. The process is governed both by warming due to solar radiation in summer and lateral influx of heat from the boundary current. On average, about 60% of the total annual heat input over the upper 1600 m is provided by lateral heat fluxes (Yashayaev and Loder 2009), but solar radiative warming is limited to the upper 200 m (Straneo 2006a). Furthermore, the fact that  
35 restratification already starts when the atmosphere is still cooling the ocean in early spring (generally in April) (Lilly et al. 1999; Avsic et al. 2006; Yashayaev and Loder 2009) and that it occurs rapidly over a large depth (Lilly et al. 1999; Avsic et al. 2006) indicates an important role of lateral heat fluxes in restratification. In this study we therefore focus on

---

<sup>1</sup>In periods of low convective activity, multi-year restratification is also important. That is however beyond the scope of this study where we focus on the restratification immediately after a deep convection winter.

the dynamics of the oceanic part of restratification (lateral fluxes) by ignoring solar radiative  
40 forcing.

The characteristics of the boundary current strongly affect restratification. Lateral fluxes  
(Figure 1a) adjust the water properties in the central Labrador Sea towards the properties  
of the very buoyant boundary current (Straneo 2006a). The boundary current water on  
the shelf is of Arctic origin and is hence cold and fresh. On the continental slope, it is  
45 of subtropical origin, and therefore relatively warm and saline. Both water masses supply  
low-density water to the interior Labrador Sea.

Early studies on restratification after deep convection focused on the efficiency of buoy-  
ancy exchange across a front (e.g. Jones and Marshall 1993; Maxworthy and Narimousa 1994;  
Jones and Marshall 1997; Legg et al. 1998). At the front surrounding the convection area  
50 a rim current develops, which becomes baroclinically unstable and generates small eddies  
with a size on the order of the Rossby deformation radius. These eddies exchange properties  
across the front and restratify the convection area. As they are formed as a result of deep  
convection, we will refer to them as Convective Eddies (CE), following Chanut et al. (2008).

After the Labrador Sea Experiment in the 1990's (LabSeaGroup 1998) it became clear  
55 that the boundary current acts as a major source of buoyancy for the replenishment of the  
dense water mass in the convected area (Lilly et al. 2003). The buoyant water is brought  
into the interior by lateral eddy fluxes (Spall 2004; Katsman et al. 2004; Straneo 2006b),  
while the dense convected water is exported out of the Labrador Sea in the boundary current  
(Straneo 2006b; Brandt et al. 2007).

60 This process is captured in a conceptual model by Straneo (2006b). With this model  
the restratifying effect of eddies originating from the boundary current was investigated.

The results of the conceptual model agree nicely with in situ measurements, indicating that restratification in the interior Labrador Sea is indeed primarily caused by eddy-driven interior-boundary current exchange. However, Straneo (2006b) did not distinguish between  
65 the contributions of different eddy types to the exchange.

There are two distinct pathways by which eddies may flux buoyancy from the boundary current into the interior. The first mechanism is a buoyancy flux associated with baroclinic eddies that form at the density front between the warm boundary current and the cold interior. Like CEs the size of these eddies is on the order of the Rossby radius of deformation,  
70 but contrary to CEs these eddies are present year round. Following Chanut et al. (2008), this eddy type will be referred to as Boundary Current Eddies (BCE).

Second, large eddies (15 to 30 km radius) are shed from the boundary current along the west coast of Greenland (Figure 1a). These eddies are referred to as Irminger Rings (IR) because of their warm and saline Irminger Water core (Lilly and Rhines 2002; Lilly et al.  
75 2003; Hatun et al. 2007). The formation of these eddies is triggered by a steepening of the slope along a portion of the western Greenland coast (Bracco and Pedlosky 2003; Wolfe and Cenedese 2006) (Figure 1a). At the downstream end of this steep slope a large eddy kinetic energy signal is detected (Prater 2002; Lilly et al. 2003; Brandt et al. 2004). IRs form spontaneously in model simulations configured with such a steep slope (Eden and Böning  
80 2002; Katsman et al. 2004; Chanut et al. 2008), while their formation can be suppressed by defining a more gentle slope for the simulation (Katsman et al. 2004; Chanut et al. 2008). Although IRs are only formed in a localized region in the eastern side of the basin, the eddies are very energetic and long-lived (Lilly et al. 2003). They travel southwestwards into the Labrador Sea interior, allowing them to bring buoyant boundary current water to the area

85 of deep convection.

The possibility to eliminate IRs from a model simulation by changing the bathymetry pattern allows a systematic investigation of their role in restratification. Katsman et al. (2004) performed two 6-month spindown simulations of the restratification season in the Labrador Sea, one with and one without IRs, in an idealized regional configuration. Based on the very slow restratification in the case where IRs were absent it was concluded that these eddies were the dominant contributors to restratification in this area. The authors only considered the contribution of CEs and IRs however, because the boundary current was too stable for BCEs to form. Chanut et al. (2008) used two 10-year equilibrium simulations in a realistic configuration to investigate the effects of CEs, BCEs and IRs on restratification. In contrast to Katsman et al. (2004), they concluded that BCEs make the dominant contribution. Because both of their simulations reached a quasi-equilibrium state, with wintertime convection and restratification over summer, and with a similar lateral heat flux into the interior, the authors concluded that the presence of IRs is not crucial for restratification.

The two equilibria in the Chanut et al. (2008) study are however very different. As at least one of the equilibria does not resemble the actual situation, the observation that the heat flux into the interior is the same does not justify conclusions on the lateral heat flux mechanisms in the real Labrador Sea. Instead, simulations of a single restratification season can be started from the same realistic end-of-winter state. The efficiency of different eddy types can be assessed by their ability to adjust this end-of-winter state to a realistic end-of-summer state within one restratification season. In this study we use this approach to address the question which eddy type dominates the lateral heat flux and we explain the opposing conclusions from previous studies.

The model configuration used in this study is described in Section 2, as well as the initial state of the model fields, the general characteristics during the spindown simulations, and a description of the simulated cases. In Section 3 the model results are discussed with respect to the rate of restratification. In Section 4 scalings are derived for the time scale of restratification for the different eddy types, which are used in Section 5 to compare the results from this study with results from earlier work. A summary of the results and conclusions is given in Section 6.

## 2. Model and initial state

In this study we used an idealized regional model for the Labrador Sea discussed below. Despite its simplicity, the model reproduced the hydrographic properties and the eddy field in the Labrador Sea well. To assess the effect of the different eddy types on restratification, three spindown simulations were performed where one or more eddy types were eliminated.

### *a. Model configuration*

The simulations in this study were performed with the MIT primitive equation model (Marshall et al. 1997) in an idealized regional configuration for the Labrador Sea (Figure 1b). The configuration was similar to the one used in Katsman et al. (2004), but the basin shape was improved and the location of the convection area was, more realistically, in the southwestern Labrador Sea.

The basin (Figure 1b and Table 1) had a maximum depth of 3000 m, which decreased

towards the boundaries to form a slope along the perimeter of the basin. Possible interactions with the Arctic via the Davis Strait have been neglected and deep boundary currents and the continental shelved were omitted. Note the steepening of the slope along the west coast of Greenland, which has been shown to be essential for the shedding of IRs (Section 1). The horizontal grid spacing was 3.75 km in both zonal and meridional directions. This is well below the Rossby radius of deformation (about 7 km in this area), so that the model is eddy resolving. In the vertical the model consisted of 15 layers with layer thickness ranging from 100 m in the upper layers to 450 m near the bottom. In the simulations, only the influence of temperature was assessed, neglecting the role of salinity for simplicity. A linear equation of state  $\rho = \rho_0 (1 - \alpha T)$  was used, with a reference density  $\rho_0$  and a constant thermal expansion coefficient  $\alpha$ . The use of a linear equation of state with temperature alone can be justified because the density of sea water is temperature dominated in the restratification season. The values of parameters used in the numerical simulations are given in Table 1.

A boundary current was formed by restoring temperature and zonal velocity south of the southern tip of Greenland (gray shaded area in Figure 1b), from where it continued cyclonically around the basin. The restoring conditions were applied over the full depth of the channel with a very short restoring time scale (40 minutes) to form a zonal flow in geostrophic balance (Katsman et al. 2004):

$$T(y, z) = T_{ref}(z) + \frac{\Delta\rho}{2\alpha\rho_0} \left(1 - \frac{z}{z_b}\right) \left[1 + \tanh\left(\frac{y - y_0}{L_y}\right)\right] \quad (1)$$

$$U(y, z) = \frac{g\Delta\rho}{4L_y f \rho_0} \frac{(z - z_b)^2}{z_b} \frac{1}{\cosh^2\left(\frac{y - y_0}{L_y}\right)} \quad (2)$$

where  $T_{ref}(z)$  is the temperature profile at the start of the spinup (based on the average den-

sity profile from a summer occupation over the southwestern part of the AR7W hydrographic section (Katsman et al. 2004). The density difference across the boundary current ( $\Delta\rho$ ) and the boundary current width ( $L_y$ ) determine the maximum boundary current velocity.   
150  $z_b$  is the bottom depth, and  $y_0$  is the meridional position of the maximum current speed, measured in distance from the south coast of Greenland.  $g$  is the acceleration due to gravity and  $f$  the Coriolis parameter. The parameter values (Table 1) were chosen such that the resulting boundary current has the properties seen in the AR7W hydrographic observations. The total transport in the boundary current was 17 Sv, in line with observational estimates   
155 (Cuny et al. 2002; Dengler et al. 2006; Fischer et al. 2010) (not taking into account deep currents associated with overflow waters not represented in this model). The maximum current velocity is  $0.56 \text{ m s}^{-1}$ , in good agreement with the observed velocity over the upper continental slope from surface drifter measurements (Cuny et al. 2002).

The use of open boundaries has been avoided by directing the boundary current behind an   
160 artificial island in the southeast of the domain, from the southern Labrador coast back to the restoring region south of Greenland (cf. Spall 2007). One IR bounced against this artificial island in one of the simulations, but as this was far away from the convection region it did not noticeably influence the results. The restoring conditions induce a continuous warming of the basin, but this is small over the limited period of the restratification season ( $0.06 \text{ }^\circ\text{C}$    
165 averaged over the interior basin in six months). The restoring conditions are the only forcing in the model; no surface fluxes are applied in any of the simulations.

*b. Setting the initial state*

Earlier idealized model studies of restratification after deep convection (Jones and Marshall 1997; Send and Käse 1998; Katsman et al. 2004) prescribed a convection region by specifying the initial density field in their simulations and an ocean at rest. However, these studies did not consider the effect of the presence of a boundary current. In order to do so, it is necessary to perform a spinup simulation first to let the warm boundary current encircle the basin and to let the eddy field develop. Once the circulation has spun up, the density field can be altered offline to prescribe a convection region representing the situation at the end of winter. In this way, all simulations of the restratification season can be started from nearly<sup>2</sup> the same conditions.

Figure 2 shows a zonal cross section of the temperature and meridional velocity at  $y = 1150$  km averaged over the last month of the spinup phase. Because the influence of salinity is neglected, the low density of the cold and fresh surface waters is represented as a warm top layer. The boundary current flows northwards along the west coast of Greenland and returns on the Canadian side in southern direction. The southward-flowing boundary current in the west is much weaker and wider and has lost part of its heat to the interior due to eddy activity. On both sides of the basin, the density and velocity structure of the boundary current compare favorably with observations (Cuny et al. 2002; Pickart and Spall 2007).

After the spin-up phase an idealized convection region was constructed synthetically

---

<sup>2</sup>At the end of the spinup phase, the temperature field in the interior displayed only minor differences between different spinup simulations. As a consequence, the amount of heat removed from the basin by constructing the convection region differs by about 1%.

by altering the temperature field of the final state of the spin-up simulation offline. The prescribed convection region (Figure 1b) has a spatially varying mixed layer in the shape of a skewed cone, with characteristics similar to the end-of-winter data published by Pickart  
 190 et al. (2002) (their Figure 12d, reproduced in Figure 1a). At each grid point inside the skewed cone, the temperature throughout the mixed layer is set equal to the temperature found at the base of the local prescribed mixed layer. The temperature field outside the convection region is unaltered (Figure 3).

We also studied the dependence of the restratification rate on the chosen shape of the  
 195 convection area. The density gradient across the front was varied by changing the shape from a cone towards a cylinder. For a wide range of the two parameters varied (mixed layer depths between 0.75 and 1.5 times the standard mixed layer depth, and frontal density gradients between 0.2 and 4 times the standard density gradient) the final conclusions on the roles of the three eddy types in restratification after deep convection (which are discussed in  
 200 the remainder of the paper) remain the same.

### *c. The eddy field*

To gain confidence that the model is realistically representing eddy processes, we examine one of our numerical simulations in which all three eddy types are resolved (see Section 2d). As a good measure of the overall eddy activity, Figure 4 gives the surface eddy speed ( $V_{EKE}$ )  
 205 calculated from the model velocity fields, as an average over the 6 months of the spindown simulation according to

$$V_{EKE} = \left( \overline{u'^2 + v'^2} \right)^{1/2}$$

where the primes denote deviations from the mean flow and the bar denotes the time mean. Lilly et al. (2003) showed  $V_{EKE}$  as inferred from satellite observations (their Figure 24). In their altimetry analysis as well as in our model the maximum  $V_{EKE}$  is found at the  
210 location where IRs are shed. From there the signal fans out in a southwesterly direction and then decays in a southerly direction, broadly indicating the path of the IRs that travel into the basin interior (8 IRs followed this pathway in our 6 month spindown simulation). The somewhat higher values in the model compared to the altimetry-based estimate are likely because of the processing of the altimeter data involving some smoothing that can lead to  
215 an underestimation of the EKE maximum. The secondary EKE maximum around  $x = 500$  km and  $y = 650$  km may be the footprints of individual eddies, an effect of the relatively short averaging period. However, a secondary maximum was also reported by Lilly et al. (2003) at this location. Overall, the pattern is in good agreement with observations.

Further support for the realism of the eddy field may be obtained by comparing the  
220 characteristics of the model-generated eddies with observations. CEs and BCEs are however too small to be captured by satellite altimetry and they are only occasionally sampled by a mooring (Lilly et al. 2003). On IRs more data is available, both remotely observed by satellites and in situ in mooring records (Lilly et al. 2003), in glider and float records (Prater 2002; Hatun et al. 2007) and, occasionally, in the WOCE AR7W hydrographic sections  
225 (Rykova et al. 2009). Their characteristics can be compared with the model results in more detail.

The IRs in the model are traced by eye from their surface temperature and sea surface elevation signal. In line with observations (Lilly et al. 2003; Prater 2002), most IRs are anticyclonic, but some dipoles and cyclonic features have been observed as well. The max-

imum velocity in the IRs ranges between 0.4 and 0.8 m s<sup>-1</sup>, occasionally reaching 0.95 m s<sup>-1</sup> when just shed off. These results are in excellent agreement with the 0.3 to 0.8 m s<sup>-1</sup> range obtained by Lilly et al. (2003). The radius of the model-generated eddies, defined by the distance between its center and the velocity maximum, ranges between 15 and 27 km, again in good agreement with the 15-30 km found by Lilly et al. (2003). As an example, Figure 5 shows the meridional velocity and temperature profile in a cross section of a representative IR from our model simulation. Its properties are in good agreement with available data (Lilly et al. 2003; Hatun et al. 2007; Rykova et al. 2009), recalling that the density in our model is temperature dependent only. The surface intensification and weakening of the currents below 500-700 m depth is also well reproduced.

#### d. Set-up of the simulations

Now that we have confidence in our model performance, we can describe three simulations designed to isolate the effects of different eddy types (Table 2). The first case, referred to as *ALL\_IN*, includes all three eddy types discussed in Section 1 and is hence the most realistic one (Figures 2 to 5 were obtained from this simulation). In the second case, *NO\_IR*, the formation of IRs is suppressed using a bathymetry with a wider slope along the west Greenland coast (Katsman et al. 2004). The effect of IRs on restratification can be assessed by comparing the *ALL\_IN* case with the *NO\_IR* case. The restratifying effect of CEs can be studied from the third case, *NO\_BC*, where the boundary current itself is left out, so that both IRs and BCEs are eliminated. The effect of BCEs on restratification may be analyzed by comparing the *NO\_BC* case with the *NO\_IR* case.

### 3. Restratification after deep convection

The results of the three spindown simulations are discussed by first analyzing the evolution of the heat content in the convection area. Next, the amount of LSW exported by the boundary current is discussed.

255 The evolution of the sea surface temperature may be used as an initial indicator of how the three eddy types act to restratify. It is displayed in Figure 6 for the three cases listed in Table 2, after three months and after six months in the simulations. The restratifying effect of the CEs alone (left panels) is clearly insufficient to warm up the Labrador Sea in half a year. The *NO\_IR* case (middle panels) shows stronger surface warming, but the warming is  
260 not fast enough. The center of the convection area is only starting to gain some heat after half a year. When IRs are present (right panels), the surface rapidly warms suggesting fast restratification of the Labrador Sea within 6 months. Also, in the right panels more violent mixing takes place: after three months the blue patch is already diluted. The mixing is caused by the high stirring rate of the IRs (see also Figure 9, which shows the concentration  
265 of a passive tracer that was initialized in the convection area only). They break up the convection area and mix on the large scale. It is likely that BCEs and CEs play a role in mixing to smaller scales and disintegrating the coherent IRs.

The importance of IRs for restratification is confirmed by the evolution of temperature with depth at the center of the convection area for the *NO\_IR* case (Figure 7a) and the  
270 *ALL\_IN* case (Figure 7b). Without IRs, the first signs of warming can be observed after three to four months, but the effect is very shallow and weak. In contrast, when IRs are present the warming already starts after 1.5 months. This is in line with in situ data (Lilly

et al. 1999; Avsic et al. 2006). Figures 6 and 7 thus point towards a dominant role of IRs in the restratification process. In the following these results will be supported quantitatively.

275 *a. Heat content change of the convection area*

An objective measure of the effect of the different eddies on restratification is the change in heat content of the convection area over time. The cone of mixed cold water prescribed as initial condition (Section 2b) has a heat deficit with respect to the unconvected state of

$$\Delta H(t) = \rho_0 c_p \int (T(x, y, z, t) - T(x, y, z, 0)) dV \quad (3)$$

where  $\rho_0$  is a reference density,  $c_p$  the heat capacity, and  $T(x, y, z, t)$  is the instantaneous  
 280 temperature at a certain location in the convection area. The integral is over the volume of the initial convection cone (Figures 1b and 3).

Figure 8 shows the evolution of the heat deficit  $\Delta H(t)$ , normalized by its initial value. The CEs replenish 25% of the initial heat deficit within six months. BCEs add another 5% to this, while IRs are able to restratify another 45%. At the end of the *ALL-IN* simulation  
 285 about 75% of the initial heat deficit is replenished. Note that the effect of the BCEs and IRs on the heat content includes export of LSW out of the convection area by the boundary current, which is discussed below.

*b. Export of LSW by the boundary current*

Export of LSW by the boundary current may be a non-negligible factor in restratification  
 290 (Brandt et al. 2007). Simulations in which a passive tracer was added inside the convective

cone illustrate this process (Figure 9). The panels show the depth-averaged tracer concentration after six months. As the *NO\_BC* case has no boundary current, the spreading of the passive tracer is entirely due to CEs.

In the *NO\_IR* case some of the LSW is exported by the boundary current, which is indicated by the blue tongue extending southwards. In our model simulation, 1.6% of the LSW was transported southwards past the  $y = 200$  km line within 6 months. In the *ALL\_IN* case about 6.7% of the convected water is exported in the boundary current. We hypothesize that this is due to the substantial stirring by IRs, which increases the interaction with the boundary current. The export in the *ALL\_IN* case is equivalent to 1 Sv, in good agreement with the amount of overturning related to the convectively transformed waters formed in the interior (Pickart and Spall 2007). Brandt et al. (2007) reported an export of newly ventilated water of about 9 Sv, but a substantial part of this is formed in the boundary current itself (see their Figures 1a and 11b). Note also that the export rate shows a large interannual variability, and that single-year simulations such as the ones in Brandt et al. (2007) and this study will not cover the whole range. Notwithstanding this uncertainty, the model results indicate that the LSW formed in the interior gives a minor contribution to the total export, as can be expected for a simulation in which convection in the boundary current is absent.

The tracer studies also shed some light on the notably small difference between the restratification rate in the *NO\_BC* case and the *NO\_IR* case. In the case without a boundary current restratification is expected to be very slow, which is supported by the model results (Figure 8). Simply adding a warm boundary current, without the Irminger Rings (*NO\_IR*), has however little effect (unless the convection area is unrealistically large and immediately adjacent to the boundary current throughout the whole Labrador Sea; not shown). The

stirring by the Irminger Rings, which act as a catalyst, is thus essential for the boundary  
 315 current to be truly effective on restratification.

## 4. Restratification time scale

To generalize the results of the numerical simulations, we derive relevant scaling relations  
 for the time it takes to restratify the convection area. This also allows for a direct comparison  
 with observations. Moreover, it provides a framework for an objective discussion of the  
 320 discrepancies between previous studies (Section 5). Jones and Marshall (1997) derived a  
 restratification time scale for a cylinder-shaped convection area with a constant ambient  
 stratification, where only CEs restratified. Here, we extend their analysis by including cone-  
 shaped convection areas. We also derive time scales for restratification by BCEs and IRs.  
 For simplicity, we consider a symmetric cone-shaped convection area rather than the skewed  
 325 shape used in the model simulations (Figures 1b and 3). Furthermore, the stratification is  
 assumed to be constant with depth as in Jones and Marshall (1997). A schematic with the  
 definitions used in this section is given in Figure 10.

### *a. Derivation of restratification time scales*

In the absence of surface forcing and other restratification mechanisms, the buoyancy  
 330 gain of a convected cone due to CEs can be expressed as (Jones and Marshall 1997, their  
 Eq. 2.6)

$$\frac{\partial}{\partial t} \int_{V_{cone}} \bar{b} dV_{cone} = - \oint \int_{-h}^0 \overline{\mathbf{v}'b'} \cdot \mathbf{n} dz dl \quad (4)$$

where  $V_{cone}$  is the volume of the cone-shaped convection area,  $\bar{b}$  is buoyancy deficit with respect to an unconvected cone,  $\overline{\mathbf{v}'b'}$  is the eddy buoyancy flux,  $\mathbf{n}$  is the normal unit vector and  $h$  is the maximum depth of the convection area. The eddy buoyancy flux is parameterized

335 as

$$\overline{\mathbf{v}'b'} = c_e \Delta b(r, z) u_0 \quad (5)$$

where  $c_e$  is a dimensionless eddy efficiency coefficient,  $\Delta b(r, z)$  is the buoyancy difference between the convection area and the ambient fluid as a function of depth and radial position (see Appendix A), and  $u_0$  is the rim current velocity. The latter may be estimated from the thermal wind balance (Jones and Marshall 1997). Combining Eqs. 4 and 5 (Appendix A)

340 yields the restratification time scale for CEs only

$$\tau_{CE} = \frac{1}{2c_e} \frac{f R_{max}^2}{N_{bg}^2 h^2} \quad (6)$$

where  $f$  is the Coriolis parameter,  $R_{max}$  is the radius of the cone-shaped convection area at the surface, and  $N_{bg}$  is the buoyancy frequency based on the ambient background stratification.

If the convection area would cover the whole basin of interest, BCEs would restratify  
 345 in the same way as CEs. The restratification time scale would then be defined by Eq. 6, with the background stratification  $N_{bg}$  replaced by the stratification of the boundary current,  $N_{bc}$ . If the convection area is smaller than the whole basin, as is the case in the Labrador Sea, BCEs exchange heat between the boundary current and the interior, thereby warming up the interior basin. This induces a sharper front around the convection area, which is  
 350 now surrounded by warmer water. Thus, they enhance the effect of CEs. We define the

stratification

$$N_{BCE}^2 = \epsilon N_{bc}^2 + (1 - \epsilon) N_{bg}^2 \quad (7)$$

which represents the enhancement of the stratification in the interior<sup>3</sup> due to the influx of boundary current water (having stratification  $N_{bc}^2$ ) by BCEs, by an amount measured by the parameter  $\epsilon$  ( $0 < \epsilon \leq 1$ ). If we assume that the heat which is brought into the interior  
 355 from the boundary current is uniformly distributed and therefore available at the edges of the convection region, we obtain a restratification time scale for the combination of CEs and BCEs (Appendix B):

$$\tau_{CE+BCE} = \frac{1}{\left(1 + \epsilon \left[ \left( \frac{N_{bc}}{N_{bg}} \right)^2 - 1 \right] \right)^2} \tau_{CE} \quad (8)$$

Note that  $\tau_{CE+BCE} < \tau_{CE}$ .

IRs mainly transport heat by carrying warm boundary current water in their core from the  
 360 coast towards the interior. The restratification time scale depends on the buoyancy brought into the convection area by an individual ring, as well as the frequency of occurrence  $f_{IR}$  of such an event:

$$\frac{\partial}{\partial t} \int_{V_{cone}} \bar{b} dV_{cone} = f_{IR} \pi r_{IR}^2 \int_{-h_{eff}}^0 \Delta b_{IR}(z) dz \quad (9)$$

In this expression,  $r_{IR}$  is the radius of the ring,  $\Delta b_{IR}(z)$  is its buoyancy anomaly (see Appendix C), and  $h_{eff}$  is the effective depth over which IRs restratify. The effective depth is  
 365 introduced because, since  $r_{IR} \ll R_{max}$ , most eddies will encounter a part of the cone with a mixed layer depth smaller than  $h$  (see Figure 10), so that only the upper part of an IR

---

<sup>3</sup>In the model simulations, the fact that restratification of the whole basin must be a multi-year effect is incorporated in the initial density field, which is made based on observations, and the spin-up of 6 months to get the boundary current - interior density gradient correct.

contributes to the restratification. On average, an individual eddy passing through the convection region will encounter a mixed layer depth equal to the mean depth over the cone ( $h_{\text{eff}} = h/3$ ). This yields a restratification time scale for IRs (Appendix C):

$$\tau_{IR} = \frac{3}{10} \frac{1}{f_{IR}} \frac{R_{max}^2}{r_{IR}^2} \left( \frac{N_{bg}}{N_{bc}} \right)^2 \quad (10)$$

370 THE EDDY EFFICIENCY COEFFICIENT  $c_e$

The main unknown in the scalings above is the eddy efficiency coefficient  $c_e$ , a measure for the rate at which baroclinic eddies transport buoyancy across a baroclinically unstable front. Estimates for  $c_e$ , based on theoretical reasoning, numerical simulations and laboratory experiments, mostly vary between  $0.02 < c_e < 0.04$  (Visbeck et al. 1996; Jones and Marshall 375 1997; Spall and Chapman 1998). Larger estimates are also found in a theoretical upper bound of  $c_e = 0.045$  (Spall and Chapman 1998), an estimate of  $c_e \approx 0.08$  by Haine and Marshall (1998), and an order of magnitude larger estimate (Legg et al. 1996) based on a quasigeostrophic model. The eddy efficiency coefficient in the *NO\_BC* simulation is  $c_e = 0.02$ , calculated based on the mean lateral eddy fluxes across the edge of the convected 380 cone by CEs. This is on the lower side of the range found in previous studies, as in our cone-shaped convection area the density change across the front is not as large as in those studies.

*b. Observation-based restratification time scales*

The restratifying effect of the three eddy types in this area can roughly be estimated  
385 using the scalings derived in Section 4a and using representative values for the Labrador  
Sea. In this section the restratification time scales are calculated from observed hydrographic  
properties of the Labrador Sea. In addition, the scalings are applied to values based on the  
model configuration and compared to the simulations results (Table 3).

CONVECTIVE EDDIES

390 If CEs were the only restratifying mechanism at play, Eq. 6 gives an estimate of the time  
it would take to restratify the whole convection area by lateral fluxes only. The convection  
area as measured in situ by Pickart et al. (2002) (Figure 1a) gives  $R_{max} = 300$  km and  
 $h = 1500$  m. To obtain an estimate of the background stratification  $N_{bg}$ , we use the mean of  
late spring occupations of the WOCE AR7W section as described in Pickart and Spall (2007):  
395 In Figure 11 the average buoyancy frequency  $N$  in the upper 1500 m of the water column  
is shown as a function of position along this section. It shows a background stratification of  
around  $N_{bg} = 1.5 \cdot 10^{-3} \text{ s}^{-1}$ . A value for the efficiency constant  $c_e$  cannot be obtained from  
measurements, as in the real ocean other eddy types are always present. It seems sensible  
to use the range most commonly found in literature ( $0.02 < c_e < 0.04$ , see Section 4a).  
400 Combining these values in Eq. 6 yields a restratification time scale  $\tau_{CE}$  for CEs alone of 0.9  
to 1.8 years, depending on the value of  $c_e$ . With  $c_e = 0.02$  as in our model,  $\tau_{CE} = 1.8$  years.

## CONVECTIVE EDDIES AND BOUNDARY CURRENT EDDIES

An exact estimate of  $\tau_{\text{CE+BCE}}$  (Eq. 8) based on observations is not feasible, as neither  $\epsilon$  nor  $N_{\text{BCE}}$  can be retrieved from measurements directly. Nevertheless, one can estimate an  
405 upper bound from the data as follows: The contribution of BCEs to restratification is largest in the southwestern part of the convection area, where the boundary current is closest and the density gradient between the boundary current and convection area is therefore strongest. Moreover, it is expected that the contribution of IRs in this part of the convection area is smallest, because they originate in the northeast and propagate from there towards the  
410 interior. If we assume no contribution from IRs on this side of the convection area and take into account that the effect of BCEs is smaller everywhere else, the enhanced stratification between the boundary current and the southwestern part of the convection area thus gives an upper bound for  $N_{\text{BCE}}$ . In Figure 11 this region is found approximately between 150 and 200 km and has an average stratification of about  $N_{\text{BCE}} = 1.75 \cdot 10^{-3} \text{ s}^{-1}$ . With  $N_{bc} = 3.0 \cdot 10^{-3}$   
415 from Figure 11 it then follows from Eq. 7 that  $\epsilon < 0.12$ . The time scale for restratification for CEs and BCEs is then more than 0.7 years. Due to the very stringent assumptions in determining an upper bound for  $N_{\text{BCE}}$  (the gradient between the convection area and the boundary current is generally much smaller than in the southwestern corner, and part of the IRs follow the boundary current around the basin to the western side (Prater 2002; Hatun  
420 et al. 2007) and the influence of IRs on this side is therefore not zero) it is likely to be significantly longer.

For a time scale estimate  $\tau_{IR}$  (Eq. 10) the work by Lilly et al. (2003) may be used to obtain the frequency of IRs reaching the convection area,  $f_{IR}$ . From their Figures 40-42 it follows that 15-45 IRs are shed from the coast each year. The number of anticyclones and dipoles, which are the eddies assumed by the authors to have positive temperature anomalies, decline, averaged over 7 years, from 30 in the northern part of the Labrador Sea to 21 in the southern part (Lilly et al. 2003, their Figure 40). With roughly 30 IRs shed per year and 70% of them reaching the southern part of the Labrador Sea, a fair estimate of  $f_{IR}$  is about  $15 \text{ yr}^{-1}$  (the estimate is lowered to 50% because the southern Labrador Sea box in Lilly et al. (2003) reaches slightly further east than the convection area). The radius of an IR is approximately 20 km (Prater 2002; Lilly et al. 2003; Hatun et al. 2007). With  $R_{max} = 300 \text{ km}$  from Pickart et al. (2002) and  $N_{bg}$  and  $N_{bc}$  taken from Figure 11, this yields a restratification time scale of 1.1 years.

*c. Model-based restratification time scales*

Now that we know the time scales of restratification for the three eddy types based on observed characteristics, we can assess whether our model simulations give similar results. The parameter values from the model used in Eqs. 6, 8 and 10 and the resulting restratification time scales are listed in the column 'model' in Table 3. ( $N_{bg}$  is based on  $T_{ref}$ ,  $N_{BCE}$  on the *NO\_IR* simulation,  $\epsilon$  is found using Eq. 7,  $f_{IR}$  is based on the fact that 8 IRs reached the convection area in 6 months in the *ALL\_IN* simulation, and  $r_{IR}$  is also found from the *ALL\_IN* simulation results.) The resulting restratification time scales are indeed in good

agreement with the ones based on observations.

The actual restratification time scale in the model simulations may be estimated by  
445 linear extrapolation of the time evolution of the heat deficit in Figure 8. The time scales  
thus obtained are listed in Table 3 under 'simulations'. Given the simplifying assumptions  
in the derivation of the scalings, the estimates are very similar. Note that none of the eddy  
types can restratify the Labrador Sea individually within one year, but as we have seen in  
Section 3 their combined effect is much more efficient.

## 450 5. Discussion

From the model simulations it is evident that IRs play an important role in the process  
of restratification in the Labrador Sea. This conclusion is in contradiction to the results  
from Chanut et al. (2008). Based on the notion that two 10-year equilibrium simulations  
(one with and one without IRs) both reach an equilibrium state, these authors concluded  
455 that BCEs play a crucial role in the restratification process, and that the importance of IRs  
is only moderate. In our view, this result does however not justify such a conclusion. A  
model can still produce a quasi-equilibrium state when a major source of buoyancy (IRs)  
is removed, but this equilibrium may not be representative for the Labrador Sea. Their  
simulation without IRs indeed displays a  $0.1^{\circ}\text{C}$  lower basin-averaged temperature compared  
460 to the simulation with IRs (Chanut et al. 2008, their Figure 4b). This is a significant  
difference representing half the annual cycle, suggesting that IRs do have a non-negligible  
impact in their simulations.

The prominent role of BCEs in the Chanut et al. (2008) study results from an overesti-

mation of the effect of BCEs, combined with an underestimation of the effect of IRs. Their  
 465 results display unrealistically deep mixed layers (2400 m) over a large part of the Labrador  
 Sea for multiple winters in a row. These are caused by the strong surface cooling that is  
 applied, which exceeds the ECMWF values by 50% (Chanut et al. 2008, their Figures 8  
 and 14). Such deep mixed layers were so far only observed in a small part of the Labrador  
 Sea basin in the early 1990's (Yashayaev 2007). Due to the large depth and extent of the  
 470 convection area the density gradient between the interior and the boundary current is very  
 large. This enhances the efficiency of BCEs in restratifying the Labrador Sea interior.

The scaling relations from Section 4a (Eq. 8) illustrate how restratification can be efficient  
 enough in their model to reach an equilibrium, despite the absence of IRs (Table 3). Beside  
 the deep mixed layers (their Figure 8a), the background stratification is also weak: the mean  
 475 stratification in the upper 1500 m is only  $N_{bg} = 0.8 \cdot 10^{-3} \text{ s}^{-1}$  (their Figure 7a). To calculate  
 $\tau_{CE+BCE}$  the stratification in the boundary current ( $N_{bc}$ ) is also required, as well as either  
 $N_{BCE}$  or the parameter  $\epsilon$ . From the temperature/density cross section we can infer that  
 the stratification in the boundary current in their simulation (their Figure 7b) is at least  
 as strong as in the climatology (their Figure 7a). We will therefore use the climatological  
 480 value of  $N_{bc} = 3.0 \cdot 10^{-3} \text{ s}^{-1}$  (Figure 11). Using  $\epsilon \approx 0.1$  from the observations, Eq. 8  
 yields a restratification time scale of 0.3 to 0.6 years (Table 3). The strongly enhanced  
 boundary current-interior density gradient thus enables restratification to be sufficiently  
 quick to restratify the Labrador Sea before the next winter even without IRs.

The contribution of IRs to restratification (Eq. 10) in the simulation of Chanut et al.  
 485 (2008) is very small because the eddies hardly reach the convection area. Their Figure 11  
 shows the tracks of IRs in two years of the simulation. Because the tracks lie too far north

compared to observations (Lilly et al. 2003), only one or two of all the IRs actually reach the southwestern part of the Labrador Sea, giving  $f_{IR} \approx 1 \text{ yr}^{-1}$ . With the other parameter values as above, the restratification time scale for IRs is 5.9 years. The time scales (Table 3) clearly show that the restratification mechanism in Chanut et al. (2008) does not match observations.

Another study on restratification by eddies in the Labrador Sea was performed by Straneo (2006b). Using a conceptual 2-layer model this study showed that lateral eddy fluxes play an important role in the restratification process in the Labrador Sea. No distinction was made however between different eddy types. Instead, the eddy flux closure in Eq. 6 was used, with  $c_e = 0.03$  based on literature. The case studied in Straneo (2006b) is a special case, since the convection area directly borders the boundary current and has the shape of a cylinder. The scalings derived for cone-shaped convection areas in this study are therefore not applicable. Alternatively, the time scale derived by Jones and Marshall (1997) for cylinder-shaped convection areas (their Equation 2.11) should be used:

$$\tau_{\text{restrat}} = \frac{3}{2c_e} \frac{R}{Nh}$$

where  $R = 230 \text{ km}$  is the radius of the convection area and  $h(= D - h_2) = 800 \text{ m}$  the depth over which lateral eddy fluxes act (Straneo 2006b, her Figure 1). The relevant stratification is here the stratification of the boundary current  $N_{bc}$ , which can be found by taking  $\frac{\partial \rho}{\partial z}$  from the center of the upper layer to the center of the lower layer ( $\Delta \rho = 0.05 \text{ kg m}^{-3}$  and  $\Delta z = 750 \text{ m}$ ), yielding  $N_{bc} = 8.0 \cdot 10^{-4} \text{ s}^{-1}$ . With these values, the restratification time scale is a very realistic 0.6 years.

Because the study by Straneo (2006b) does not distinguish between different eddy types,

we should compare its restratification time scale to a time scale based on our model with all three eddy types included. Assuming a linear superposition of the effects of the eddies, the evolution of the buoyancy in the convected cone is given by a combination of Eqs. 4 and 9:

$$\frac{\partial}{\partial t} \int_{V_{cone}} \bar{b} dV_{cone} = - \oint \int_{-h}^0 \overline{\mathbf{v}'b'} \cdot \mathbf{n} dz dl + f_{IR} \pi r_{IR}^2 \int_{-h_{eff}}^0 \Delta b_{IR}(z) dz \quad (11)$$

A restratification time scale for the combined effect of all three eddy types can be derived (see Eqs. A4, B3 and C3):

$$\frac{1}{\tau_{ALL}} = \frac{4}{N_{bg}^2 h} \left( \frac{c_e (\epsilon N_{bc}^2 + [1 - \epsilon] N_{bg}^2)^2 h^3}{2 f R_{max}^2} + \frac{5}{6} f_{IR} \frac{r_{IR}^2}{R_{max}^2} N_{bc}^2 h \right) \quad (12)$$

With parameter values from our study (Table 3, 'model' column) this yields a restratification time of 0.6 years, in good agreement with the estimate from Straneo (2006b).

## 515 6. Summary and Conclusions

The contributions of three different eddy types (Convective Eddies, Boundary Current Eddies and Irminger Rings, see Section 1) to restratification after deep convection in the Labrador Sea are assessed using simulations of the restratification season with an idealized numerical model. The model configuration is comparable to the one used by Katsman et al. (2004), but highly improved in terms of basin shape and location and shape of the convection area. Furthermore, the analysis was expanded to include the effect of Boundary Current Eddies.

Three different cases were studied: one with only Convective Eddies, one with Convective Eddies and Boundary Current Eddies, and one with all three eddy types. The model results clearly show an essential role of Irminger Rings in the restratification process. Convective

Eddies and Boundary Current Eddies together only replenish 30% of the initial heat loss, while IRs add another 45% (Figure 8). Part of the effectiveness of Irminger Rings in restratification is due to enhanced interaction with the boundary current: In the simulation with Irminger Rings, the transport of convected water out of the convection region is four times larger than in the simulation without Irminger Rings. Also, IRs stir the convected water through the basin, thereby facilitating mixing by the smaller eddies. Thus, while we argue that IRs are required for restratification in this region, they may need the smaller eddies to be genuinely effective.

Simple theoretical scalings, used to assess the time it takes the three different eddy types to restratify the convective region, lead to the same conclusion (Table 3). The estimated restratification time scales show that none of the three eddy types can restratify the Labrador Sea by themselves during one restratification season. The contribution of IRs (restratification time scale of 1 year and 1 month) is slightly larger than the contribution of CEs and BCEs together (restratification time scale of more than 1 year and 2 months). When all three eddy types contribute to the restratification process, the estimated time scale is a realistic 7 months.

A few interesting questions for further research have arisen from this study. First, it was shown that IRs are an efficient mixer, which suggests that their interaction with the other eddy types may not be a simple linear superposition. Although the scalings, which are based on the assumption of this linear superposition, give very reasonable results, the nature of the interaction might be important for a proper representation of the restratification process. Also, the pathways of the IRs are apparently of vital importance to model the restratification appropriately. It is as yet unclear what determines these pathways and why they are different

in the Chanut et al. (2008) model. Third, the frequency of IRs reaching the convection area  
550 shows a seasonal and interannual variability in reality. The question how that affects the  
restratification process is still unanswered. Last, and perhaps most importantly, IRs are not  
resolved in the current generation of global climate models. As the eddies play an important  
role in restratification in this area, they should be adequately parameterized.

*Acknowledgments.*

555 This research was funded by a grant from the NWO/SRON User Support Programme  
Space Research. The useful discussions with Bob Pickart, Mike Spall and Fiamma Straneo  
are highly appreciated. We are particularly grateful for the in situ data provided by Bob  
Pickart.

## APPENDIX A

560

### Derivation of $\tau_{CE}$

The evolution of the buoyancy deficit in the convection area is equal to the buoyancy flux through the lateral surface of the cone by CEs:

$$\frac{\partial}{\partial t} \int_{V_{cone}} \bar{b} dV_{cone} = - \oint \int_{-h}^0 \overline{\mathbf{v}'b'} \cdot \mathbf{n} dz dl \quad (A1)$$

where the left hand side represent the change in buoyancy in time, integrated over the volume  
 565 of the cone. The buoyancy flux through the sides of the cone  $\overline{\mathbf{v}'b'}$  is parameterized by

$$\overline{\mathbf{v}'b'} = c_e \Delta b(r, z) u_0 \quad (A2)$$

with  $c_e$  an eddy efficiency coefficient,  $\Delta b(r, z)$  the buoyancy difference between the convection area and the ambient fluid

$$\Delta b(r, z) = N_{bg}^2 h \left(1 + \frac{z}{h}\right) \left(1 - \frac{r}{R_{max} (1 + z/h)}\right) \quad (A3)$$

as a function of horizontal position  $r$  and vertical position  $z$  in the convected cone.  $N_{bg}$  is the background stratification,  $h$  the maximum convection depth, and  $R_{max}$  the radius of the  
 570 cone at the sea surface.  $u_0$  is the rim current velocity at the surface, which can be found from the thermal wind balance as follows:

$$\frac{\partial u}{\partial z} = \frac{1}{f} \frac{\partial \rho}{\partial r} \approx \frac{1}{f} \frac{\Delta b(0, z)}{R_{max} (1 + z/h)} = \frac{1}{f} \frac{N_{bg}^2 h}{R_{max}}$$

with density  $\rho$ . Integrating over the vertical direction gives the velocity as a function of  $z$ :

$$\begin{aligned}\int \frac{\partial u}{\partial z} dz &= \frac{1}{f} \frac{N_{bg}^2 h^2}{R_{max}} \left( \frac{z}{h} + c \right) \\ \Rightarrow u(z) &= \frac{1}{f} \frac{N_{bg}^2 h^2}{R_{max}} \left( \frac{z}{h} + c \right)\end{aligned}$$

The integration constant can be obtained by ensuring that the vertical integral of  $u$  over the mixed layer is zero:

$$\begin{aligned}\int_{-h}^0 u(z) dz &= \frac{1}{f} \frac{N_{bg}^2 h^2}{R_{max}} \left( \frac{1}{h} \int_{-h}^0 z dz + c \int_{-h}^0 dz \right) \\ &= \frac{1}{f} \frac{N_{bg}^2 h^2}{R_{max}} \left( -\frac{1}{2}h + c h \right) = 0 \Rightarrow c = \frac{1}{2} \\ u(z) &= \frac{N_{bg}^2 h^2}{f R_{max}} \left( \frac{z}{h} + \frac{1}{2} \right)\end{aligned}$$

The right hand side of Eq. A1 is then, after dividing over the volume of the cone:

$$\begin{aligned}&\frac{1}{V_{cone}} 2\pi \int_{z=-h}^0 \int_{r=0}^{R_{max}(1+\frac{z}{h})} c_e \Delta b(r, z) u(z=0) dr dz \\ &= \frac{2\pi}{\frac{1}{3}\pi R_{max}^2 h} \int_{z=-h}^0 \int_{r=0}^{R_{max}(1+\frac{z}{h})} c_e N_{bg}^2 h \left(1 + \frac{z}{h}\right) \left(1 - \frac{r}{R_{max}} \left(1 + \frac{z}{h}\right)^{-1}\right) \frac{1}{2} \frac{N_{bg}^2 h^2}{f R_{max}} dr dz \\ &= \frac{c_e}{2} \frac{N_{bg}^4 h^3}{f R_{max}^2}\end{aligned}$$

The integral on the left hand side of Eq. A1 is, after dividing over the volume of the cone:

$$\begin{aligned}&\frac{1}{V_{cone}} 2\pi \int_{z=-h}^0 \int_{r=0}^{R_{max}(1+\frac{z}{h})} r \Delta b(r, z) dr dz \\ &= \frac{2\pi}{\frac{1}{3}\pi R_{max}^2 h} \int_{z=-h}^0 \int_{r=0}^{R_{max}(1+\frac{z}{h})} r N_{bg}^2 h \left(1 + \frac{z}{h}\right) \left(1 - \frac{r}{R_{max}} \left(1 + \frac{z}{h}\right)^{-1}\right) dr dz \\ &= \frac{1}{4} N_{bg}^2 h\end{aligned}$$

575 The time scale can now be found by equating the right and left hand side of Eq. A1:

$$\begin{aligned}\frac{c_e}{2} \frac{N_{bg}^4 h^3}{f R_{max}^2} &= \frac{1}{\tau_{CE}} \frac{1}{4} N_{bg}^2 h \\ \tau_{CE} &= \frac{1}{2c_e} \frac{f R_{max}^2}{N_{bg}^2 h^2}\end{aligned}\tag{A4}$$

## APPENDIX B

### Derivation of $\tau_{\text{CE+BCE}}$

580 Eq. A1 is also applicable to restratification by BCEs. The left hand side, i.e. the initial buoyancy deficit, is unchanged, but the rate of restratification differs. The closure from Eq. A2 is still valid, but the buoyancy difference  $\Delta b(r, z)$  is now larger. BCEs basically warm up the basin surrounding the convection area, thereby enhancing the effect of CEs. We therefore introduce a new stratification

$$N_{\text{BCE}}^2 = \epsilon N_{bc}^2 + (1 - \epsilon) N_{bg}^2 \quad (\text{B1})$$

585 with  $N_{bc}$  the stratification in the boundary current and  $\epsilon$  a parameter ( $0 < \epsilon \leq 1$ ). The buoyancy difference (Eq. A3) is then

$$\Delta b(r, z) = (\epsilon N_{bc}^2 + (1 - \epsilon) N_{bg}^2) h \left(1 + \frac{z}{h}\right) \left(1 - \frac{r}{R_{max} \left(1 + \frac{z}{h}\right)}\right) \quad (\text{B2})$$

Analogous to the case of CEs this gives the following velocity profile based on the thermal wind balance:

$$u(z) = \frac{(\epsilon N_{bc}^2 + (1 - \epsilon) N_{bg}^2) h^2}{f R_{max}} \left(\frac{z}{h} + \frac{1}{2}\right)$$

The right hand side of Eq. A1 for the BCE case is thus, after division by the volume of the cone

$$\begin{aligned}
& \frac{1}{V_{cone}} 2\pi \int_{z=-h}^0 \int_{r=0}^{R_{max}(1+\frac{z}{h})} c_e \Delta b(r, z) u(z=0) dr dz \\
&= \frac{2\pi}{\frac{1}{3}\pi R_{max}^2 h} \int_{z=-h}^0 \int_{r=0}^{R_{max}(1+\frac{z}{h})} \\
& \left[ c_e (\epsilon N_{bc}^2 + (1-\epsilon) N_{bg}^2) h \left(1 + \frac{z}{h}\right) \left(1 - \frac{r}{R_{max}} \left(1 + \frac{z}{h}\right)^{-1}\right) \frac{1}{2} \frac{(\epsilon N_{bc}^2 + (1-\epsilon) N_{bg}^2) h^2}{f R_{max}} \right] dr dz \\
&= \frac{c_e (\epsilon N_{bc}^2 + [1-\epsilon] N_{bg}^2)^2 h^3}{2 f R_{max}^2}
\end{aligned}$$

Equating the left and right hand side of Eq. A1 yields  $\tau_{CE+BCE}$ :

$$\begin{aligned}
\frac{c_e (\epsilon N_{bc}^2 + [1-\epsilon] N_{bg}^2)^2}{2 f R_{max}^2} &= \frac{1}{\tau_{CE+BCE}} \frac{1}{4} N_{bg}^2 h \\
\frac{1}{\tau_{CE+BCE}} &= 2c_e \frac{h^2}{f R_{max}} \frac{(\epsilon N_{bc}^2 + [1-\epsilon] N_{bg}^2)^2}{N_{bg}^2} \\
&= \tau_{CE} \left( 1 - \epsilon \left[ 1 - \left( \frac{N_{bc}}{N_{bg}} \right)^2 \right] \right)^2 \\
\tau_{CE+BCE} &= \frac{1}{\left( 1 + \epsilon \left[ \left( \frac{N_{bc}}{N_{bg}} \right)^2 - 1 \right] \right)^2} \tau_{CE} \tag{B3}
\end{aligned}$$

590

## APPENDIX C

### Derivation of $\tau_{IR}$

In the case of restratification by IRs the right-hand side of Eq. A2 is not appropriate to estimate the eddy flux. IRs carry buoyant water from the boundary current into the interior.

595

An appropriate way to describe the influx of buoyancy by IRs is therefore to estimate the buoyancy brought into the convected cone by an individual ring of radius  $r_{IR}$ , and account for the frequency  $f_{IR}$  of occurrence of such an event:

$$\frac{\partial}{\partial t} \int_{V_{cone}} \bar{b} dV_{cone} = f_{IR} \pi r_{IR}^2 \int_{-h_{eff}}^0 \Delta b_{IR}(z) dz \quad (C1)$$

For an explanation of  $h_{eff}$  see Section 4a. The initial buoyancy deficit, given on the left hand side of Eq. C1, is the same as before ( $\frac{1}{4} N_{bg}^2 h$ ). On the right hand side the buoyancy difference  $\Delta b_{IR}(z)$  is given by

$$\Delta b_{IR}(z) = N_{bc}^2 h \left( 1 + \frac{z}{h} \right) \quad (C2)$$

The right hand side of equation of Eq. C1 is thus, after dividing by the volume of the cone:

$$\begin{aligned} \frac{1}{V_{cone}} f_{IR} \pi r_{IR}^2 \int_{-h_{eff}}^0 \Delta b_{IR}(z) dz &= \frac{1}{\frac{1}{3} \pi R_{max}^2 h} f_{IR} \pi r_{IR}^2 \int_{-h_{eff}}^0 N_{bc}^2 h \left( 1 + \frac{z}{h} \right) dz \\ &= \frac{5}{6} f_{IR} \frac{r_{IR}^2}{R_{max}^2} N_{bc}^2 h \end{aligned}$$

Equating the left and right hand side of Eq. C1 gives  $\tau_{IR}$ :

$$\begin{aligned} \frac{5}{6} f_{IR} \frac{r_{IR}^2}{R_{max}^2} N_{bc}^2 h &= \frac{1}{\tau_{IR}} \frac{1}{4} N_{bg}^2 h \\ \tau_{IR} &= \frac{3}{10} \frac{1}{f_{IR}} \frac{R_{max}^2}{r_{IR}^2} \left( \frac{N_{bg}}{N_{bc}} \right)^2 \end{aligned} \quad (C3)$$

## REFERENCES

- Avsic, T., J. Karstensen, U. Send, and J. Fischer, 2006: Interannual variability of newly formed Labrador Sea Water from 1994 to 2005. *Geophysical Research Letters*, **33**, doi:10.1029/2006GL026913.
- Biastoch, A., C. Böning, and J. Getzlaff, 2008: Causes of interannual-decadal variability in the meridional overturning circulation of the midlatitude north atlantic ocean. *Journal of climate*, **21**, 6599–6615.
- Bower, A., M. Lozier, S. Gary, and C. Böning, 2009: Interior pathways of the North Atlantic meridional overturning circulation. *Nature*, **459**, doi:10.1038/nature07979.
- Bracco, A. and J. Pedlosky, 2003: Vortex generation by topography in locally unstable baroclinic flows. *Journal of Physical Oceanography*, **33**, 207–219.
- Brandt, P., A. Funk, L. Czeschel, C. Eden, and C. Böning, 2007: Ventilation and transformation of Labrador Sea Water and its rapid export in the deep Labrador Current. *Journal of Physical Oceanography*, **37**, 946–961.
- Brandt, P., F. Schott, A. Funk, and C. Martins, 2004: Seasonal to interannual variability of the eddy field in the Labrador Sea from satellite altimetry. *Journal of Geophysical Research*, **109**, doi:10.1029/2002JC001551.
- Chanut, J., B. Barnier, W. Large, L. D. T. Penduff, and P. M. J.M. Molines, 2008: Mesoscale

eddies in the Labrador Sea and their contribution to convection and restratification. *Journal of Physical Oceanography*, **38**, 1617–1643.

625 Clarke, R. and J. Gascard, 1983: The formation of Labrador Sea Water. Part I: Large-scale processes. *Journal of Physical Oceanography*, **13**, 1764–1778.

Cuny, J., P. Rhines, P. Niiler, and S. Bacon, 2002: Labrador Sea boundary currents and the fate of the Irminger Sea Water. *Journal of Physical Oceanography*, **32**, 627–647.

Dengler, M., J. Fischer, F. Schott, and R. Zantopp, 2006: Deep Labrador Current and its  
630 variability in 1996-2005. *Geophysical Research Letters*, **33**, L21S06.

Dickson, R. R., J. Lazier, J. Meincke, P. Rhines, and J. Swift, 1996: Long-term coordinated changes in the convective activity of the North Atlantic. *Progress in Oceanography*, **38**, 241–295.

Eden, C. and C. Böning, 2002: Sources of eddy kinetic energy in the Labrador Sea. *Journal  
635 of Physical Oceanography*, **32**, 3346–3363.

Eden, C. and J. Willebrand, 2001: Mechanism of Interannual to Decadal Variability of the North Atlantic Circulation. *Journal of Climate*, **14**, 2266–2280.

Fischer, J., M. Visbeck, R. Zantopp, and N. Nunes, 2010: Interannual to decadal variability of outflow from the Labrador Sea. *Geophysical Research Letters*, **37**, L24 610.

640 Haine, T. and J. Marshall, 1998: Gravitational, symmetric, and baroclinic instability of the ocean mixed layer. *Journal of Physical Oceanography*, **28**, 634–658.

- Hatun, H., C. Eriksen, and P. Rhines, 2007: Buoyant eddies entering the Labrador Sea observed with gliders and altimetry. *Journal of Physical Oceanography*, **37**, 2838–2854.
- Jones, H. and J. Marshall, 1993: Convection with rotation in a neutral ocean: A study of  
645 open-ocean deep convection. *Journal of Physical Oceanography*, **23**, 1009–1039.
- Jones, H. and J. Marshall, 1997: Restratification after deep convection. *Journal of Physical Oceanography*, **27**, 2276–2287.
- Katsman, C., M. Spall, and R. Pickart, 2004: Boundary current eddies and their role in the restratification of the Labrador Sea. *Journal of Physical Oceanography*, **34**, 1967–1983.
- 650 Kieke, D., M. Rhein, L. Stramma, W. Smethie, J. Bullister, and D. LeBel, 2007: Changes in the pool of Labrador Sea Water in the subpolar North Atlantic. *Geophysical Research Letters*, **34**, doi:10.1029/2006GL028959.
- LabSeaGroup, 1998: The Labrador Sea deep convection experiment. *Bulletin of the American Meteorological Society*, **79**, 2033–2058.
- 655 Lazier, J., 1973: The renewal of Labrador Sea Water. *Deep-Sea Research*, **20**, 341–353.
- Lazier, J., R. Hendry, A. Clarke, I. Yashayaev, and P. Rhines, 2002: Convection and restratification in the Labrador Sea. *Deep-Sea Research I*, **49**, 1819–1835.
- Legg, S., H. Jones, and M. Visbeck, 1996: A heton perspective of baroclinic eddy transfer in localized open ocean convection. *Journal of Physical Oceanography*, **26**, 2251–2266.
- 660 Legg, S., J. McWilliams, and J. Gao, 1998: Localization of deep convection by a mesoscale eddy. *Journal of Physical Oceanography*, **28**, 944–970.

Lilly, J. and P. Rhines, 2002: Coherent eddies in the Labrador Sea observed from a mooring. *Journal of Physical Oceanography*, **32**, 585–598.

665 Lilly, J., P. Rhines, R. Davis, J. Lazier, F. Schott, and D. Farmer, 1999: Observing deep convection in the Labrador Sea during winter 1994/95. *Journal of Physical Oceanography*, **29**, 2065–2098.

Lilly, J., P. Rhines, F. Schott, K. Lavender, J. Lazier, U. Send, and E. D’Asaro, 2003: Observations of the Labrador Sea eddy field. *Progress in Oceanography*, **59**, 75–176.

670 Marshall, J., A. Adcroft, C. Hill, L. Perelman, and C. Heisey, 1997: A finite-volume, incompressible Navier Stokes model for studies of the ocean on parallel computers. *Journal of Geophysical Research*, **102**, 5753–5766.

Marshall, J. and F. Schott, 1999: Open-ocean convection: Observations, theory, and models. *Review of Geophysics*, **37**, 1–64.

675 Maxworthy, T. and S. Narimousa, 1994: Unsteady, turbulent convection into a homogeneous, rotating fluid with oceanographic applications. *Journal of Geophysical Research*, **24**, 865–887.

Pickart, R. and M. Spall, 2007: Impact of Labrador Sea convection on the North Atlantic meridional overturning circulation. *Journal of Physical Oceanography*, **37**, 2207–2227.

680 Pickart, R., D. Torres, and R. Clarke, 2002: Hydrography of the Labrador Sea during active convection. *Journal of Physical Oceanography*, **32**, 428–457.

Prater, M., 2002: Eddies in the Labrador Sea as observed by profiling RAFOS floats and remote sensing. *Journal of Physical Oceanography*, **32**, 411–427.

Rykova, T., F. Straneo, J. Lilly, and I. Yashayaev, 2009: Irminger Current anticyclones in the Labrador Sea observed in the hydrographic record, 1990-2004. *Journal of Marine Research*, **67**, 361–384.

Send, U. and R. Käse, 1998: Parameterization of processes in deep convection regimes. *Ocean modelling and parameterization*, E. Chassignet and J. Verron, Eds., Kluwer Academic Publishers, 191–214.

Spall, M., 2004: Boundary currents and water mass transformation in marginal seas. *Journal of Physical Oceanography*, **34**, 1197–1213.

Spall, M., 2007: Circulation and water mass transformation in a model of the Chukchi Sea. *Journal of Geophysical Research*, **112**, doi:10.1029/2005JC003364.

Spall, M. and D. Chapman, 1998: On the efficiency of baroclinic eddy heat transport across narrow fronts. *Journal of Physical Oceanography*, **28**, 2275–2287.

Straneo, F., 2006a: Heat and freshwater transport through the central Labrador Sea. *Journal of Physical Oceanography*, **36**, 606–628.

Straneo, F., 2006b: On the connection between dense water formation, overturning, and poleward heat transport in a convective basin. *Journal of Physical Oceanography*, **36**, 1822–1840.

700 Visbeck, M., J. Marshall, and H. Jones, 1996: Dynamics of isolated convective regions in  
the ocean. *Journal of Physical Oceanography*, **26**, 1721–1734.

Wolfe, C. and C. Cenedese, 2006: Laboratory experiments on eddy generation by a buoyant  
coastal current flowing over variable bathymetry. *Journal of Physical Oceanography*, **36**,  
395–411.

705 Yashayaev, I., 2007: Hydrographic changes in the Labrador Sea, 1960-2005. *Progress in*  
*Oceanography*, **73**, 242–276.

Yashayaev, I. and J. Loder, 2009: Enhanced production of Labrador Sea Water in 2008.  
*Geophysical Research Letters*, **36**, doi:10.1029/2008GL036162.

## List of Tables

710	1	Standard parameter values.	41
	2	Overview of three cases that are studied and the eddy types resolved in these simulations.	42
715	3	Restratification time scales and the parameter values used to calculated them. The time scales under 'Observations', 'Model', and 'Chanut et al. (2008)' are based on Eqs. 6, 8 and 10. The time scales under 'Simulations' are found by extrapolation of the lines in Figure 8: $\tau_{CE}$ from the <i>NO_BC</i> simulation, $\tau_{BCE+CE}$ from the <i>NO_IR</i> simulation, and $\tau_{IR}$ from the difference between the <i>ALL_IN</i> and the <i>NO_IR</i> simulations.	43

basin width (zonal)	945 km
basin length (meridional)	1417.5 km
channel width	112.5 km
horizontal eddy viscosity	$0.9 \times 10^8 \text{ m}^4\text{s}^{-1}$
horizontal diffusion coefficient	$0.5 \times 10^8 \text{ m}^4\text{s}^{-1}$
vertical eddy viscosity	$1.0 \times 10^5 \text{ m}^2\text{s}^{-1}$
vertical diffusion coefficient	$1.0 \times 10^5 \text{ m}^2\text{s}^{-1}$
$\rho_0$	$1028 \text{ kg m}^{-3}$
$\alpha$	$2.0 \times 10^{-4} \text{ }^\circ\text{C}^{-1}$
$\Delta\rho$	$-0.26 \text{ kg m}^{-3}$
$L_y$	22.5 km
$y_0$	22.5 km
$f$	$1.26 \times 10^{-4} \text{ s}^{-1}$
$g$	$9.81 \text{ m s}^{-2}$

Table 1: Standard parameter values.

Simulation name	Description	Resolved eddies		
		IR	BCE	CE
<i>ALL_IN</i>	unstable BC, steep slope	+	+	+
<i>NO_IR</i>	unstable BC, wide slope	-	+	+
<i>NO_BC</i>	no BC	-	-	+

Table 2: Overview of three cases that are studied and the eddy types resolved in these simulations.

	Observations	Model	Simulations	Chanut et al. (2008)
$c_e$	0.02 - 0.04	0.02		0.02 - 0.04
$N_{bg}$ ( $s^{-1}$ )	$1.5 \cdot 10^{-3}$	$1.6 \cdot 10^{-3}$		$0.8 \cdot 10^{-3}$
$R_{max}$ (km)	300	300		350
$h$ (m)	1500	1500		2400
$N_{BCE}$ ( $s^{-1}$ )	$1.75 \cdot 10^{-3}$	$1.7 \cdot 10^{-3}$		-
$N_{bc}$ ( $s^{-1}$ )	$3.0 \cdot 10^{-3}$	$3.0 \cdot 10^{-3}$		$3.0 \cdot 10^{-3}$
$\epsilon$	< 0.12	0.05		0.1
$f_{IR}$ (per year)	15	16		1
$r_{IR}$ (km)	20	20		20
$\tau_{CE}$ (years)	0.9 - 1.8	1.6	2.0	1.7 - 3.3
$\tau_{BCE+CE}$ (years)	> 0.7	1.3	1.8	0.3 - 0.6
$\tau_{IR}$ (years)	1.1	1.2	1.5	5.9

Table 3: Restratification time scales and the parameter values used to calculate them. The time scales under 'Observations', 'Model', and 'Chanut et al. (2008)' are based on Eqs. 6, 8 and 10. The time scales under 'Simulations' are found by extrapolation of the lines in Figure 8:  $\tau_{CE}$  from the *NO\_BC* simulation,  $\tau_{BCE+CE}$  from the *NO\_IR* simulation, and  $\tau_{IR}$  from the difference between the *ALL\_IN* and the *NO\_IR* simulations.

## List of Figures

- 720 1 (a) Map of the Labrador Sea, with a schematic representation of the boundary  
current and the three eddy types (WGC West Greenland Current, IC Irminger  
Current, LC Labrador Current, IR Irminger Ring, BCE Boundary Current  
Eddy, CE Convective Eddy). The dashed lines are the 500 to 2500 m isobaths  
(contour interval of 500 m). The mixed layer depth in the winter of 1997  
725 is shaded in color (Pickart et al. 2002). (b) Model domain and idealized  
bathymetry (contour interval is 500 m). The domain shape is roughly based  
on the 1000 m isobath in (a) to exclude the shelves. A boundary current is  
forced at the southern tip of Greenland by restoring conditions for temperature  
and velocity, applied in the shaded area. The L-shaped island in the southeast  
730 guides the flow back towards the restoring region. The mixed layer depth in  
the idealized convection area is shaded in color. 47
- 2 Zonal cross section of the basin at  $y = 1150$  km, time-averaged over the last  
month of the 6 month spin-up phase. Temperature ( $^{\circ}\text{C}$ ) is shaded in color  
and the meridional velocity is overlaid (contour interval is  $0.1 \text{ m s}^{-1}$ , dashed  
735 represents southward flow). The Canadian (Greenland) side is on the left  
(right). 48
- 3 The convection area in the model, constructed based on end-of-winter data  
(see Figure 1) in the form of a skewed cone. (a) Plan view. Gray scale is  
temperature above  $5.4^{\circ}\text{C}$ . The IR signals are clearly visible in the northeast.  
740 (b) Zonal cross section at  $y = 700$  km. Contours indicate temperature ( $^{\circ}\text{C}$ ). 49

4	Surface eddy speed ( $V_{EKE}$ ) averaged over the 6 month spindown simulation (cm s <sup>-1</sup> ). The field is smoothed with a two dimensional 3-point boxcar filter.	50
5	Zonal cross section of an example Irminger Ring from the model ( $y = 630$ km, $t = 3$ months, see upper right panel of Figure 6). (a) Meridional velocity (contour interval is 0.25 m s <sup>-1</sup> ). (b) Temperature (contour interval is 0.5°C).	51
745		
6	Snapshot of the surface temperature field (°C) for the three different cases. Left: <i>NO_BC</i> . Middle: <i>NO_IR</i> . Right: <i>ALL_IN</i> . Upper row: $t = 3$ months. Lower row: $t = 6$ months.	52
7	Time series of the temperature evolution averaged over an area in the center of the convection area ( $x = 350-450$ km, $y = 825-925$ km) for the (a) <i>NO_IR</i> case and the (b) <i>ALL_IN</i> case. Contours are plotted every 0.1°C.	53
750		
8	Heat content deficit of the convection area normalized by its initial value. The latter is defined as the reduction in the heat content that arises from the construction of the convection area (Section 2b). A zero heat content anomaly implies that the heat content of the convected cone has become exactly equal to the heat content of a cone before convection. Solid line: <i>ALL_IN</i> . Dashed line: <i>NO_IR</i> . Dash-dotted line: <i>NO_BC</i> .	54
755		
9	Depth-averaged concentration of a passive tracer after 6 months in the spindown simulations (a) <i>NO_BC</i> (b) <i>NO_IR</i> (c) <i>ALL_IN</i> . The tracer was initialized to 1 inside the convected area and to 0 in the remainder of the domain.	55
760		
10	Definitions of the variables used in the derivations of the restratification time scales in Section 4a.	56

11 Buoyancy frequency averaged over the upper 1500 m of the water column from a mean late spring section over the 1990's (Pickart and Spall 2007). The shaded areas marked by A are used to determine  $N_{bc}$ , the area marked by B is used to determine  $N_{BCE}$ , and  $N_{bg}$  is found from the area marked by C.

57

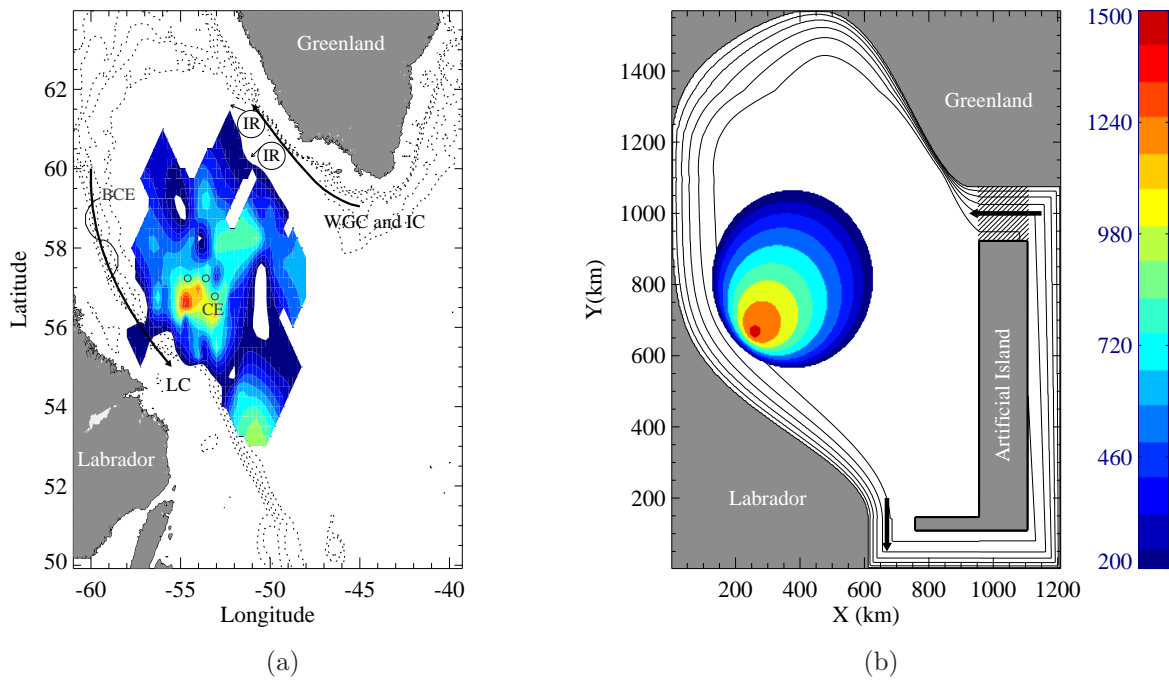


Figure 1: (a) Map of the Labrador Sea, with a schematic representation of the boundary current and the three eddy types (WGC West Greenland Current, IC Irminger Current, LC Labrador Current, IR Irminger Ring, BCE Boundary Current Eddy, CE Convective Eddy). The dashed lines are the 500 to 2500 m isobaths (contour interval of 500 m). The mixed layer depth in the winter of 1997 is shaded in color (Pickart et al. 2002). (b) Model domain and idealized bathymetry (contour interval is 500 m). The domain shape is roughly based on the 1000 m isobath in (a) to exclude the shelves. A boundary current is forced at the southern tip of Greenland by restoring conditions for temperature and velocity, applied in the shaded area. The L-shaped island in the southeast guides the flow back towards the restoring region. The mixed layer depth in the idealized convection area is shaded in color.

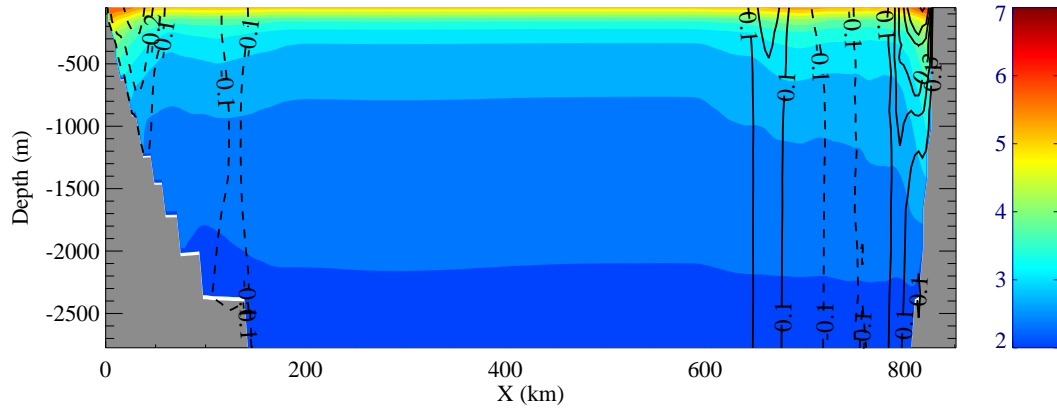


Figure 2: Zonal cross section of the basin at  $y = 1150$  km, time-averaged over the last month of the 6 month spin-up phase. Temperature ( $^{\circ}\text{C}$ ) is shaded in color and the meridional velocity is overlaid (contour interval is  $0.1 \text{ m s}^{-1}$ , dashed represents southward flow). The Canadian (Greenland) side is on the left (right).

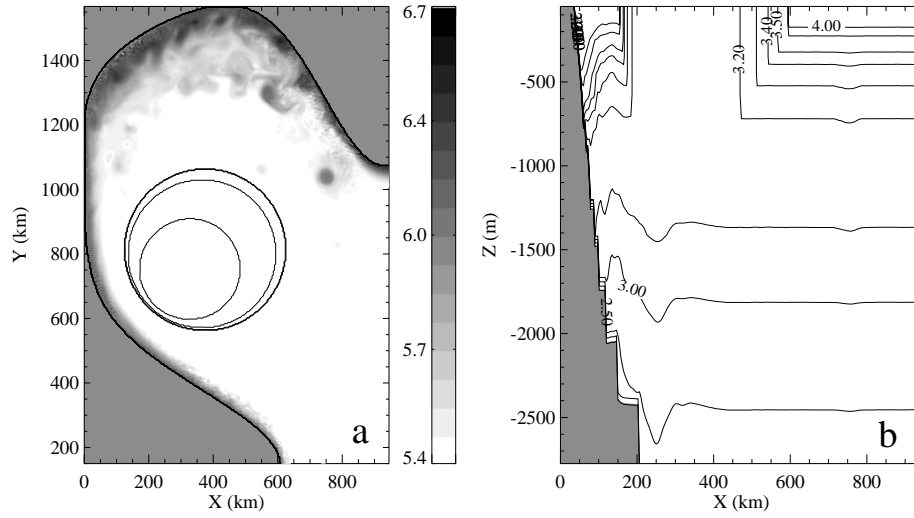


Figure 3: The convection area in the model, constructed based on end-of-winter data (see Figure 1) in the form of a skewed cone. (a) Plan view. Gray scale is temperature above 5.4°C. The IR signals are clearly visible in the northeast. (b) Zonal cross section at  $y = 700$  km. Contours indicate temperature ( $^{\circ}\text{C}$ ).

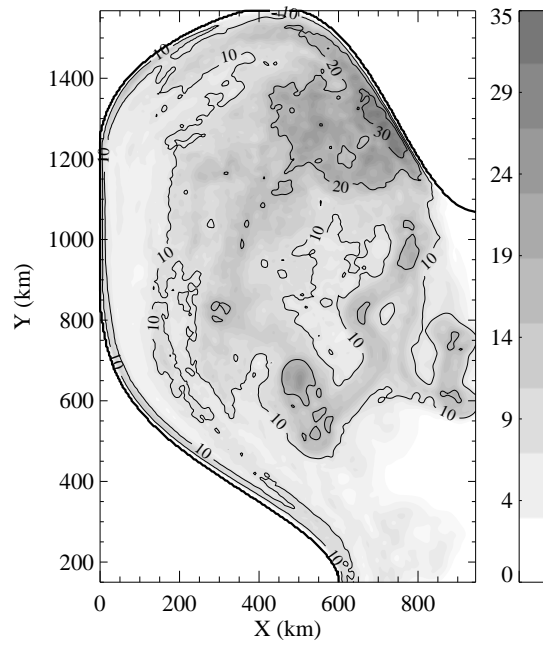


Figure 4: Surface eddy speed ( $V_{EKE}$ ) averaged over the 6 month spindown simulation ( $\text{cm s}^{-1}$ ). The field is smoothed with a two dimensional 3-point boxcar filter.

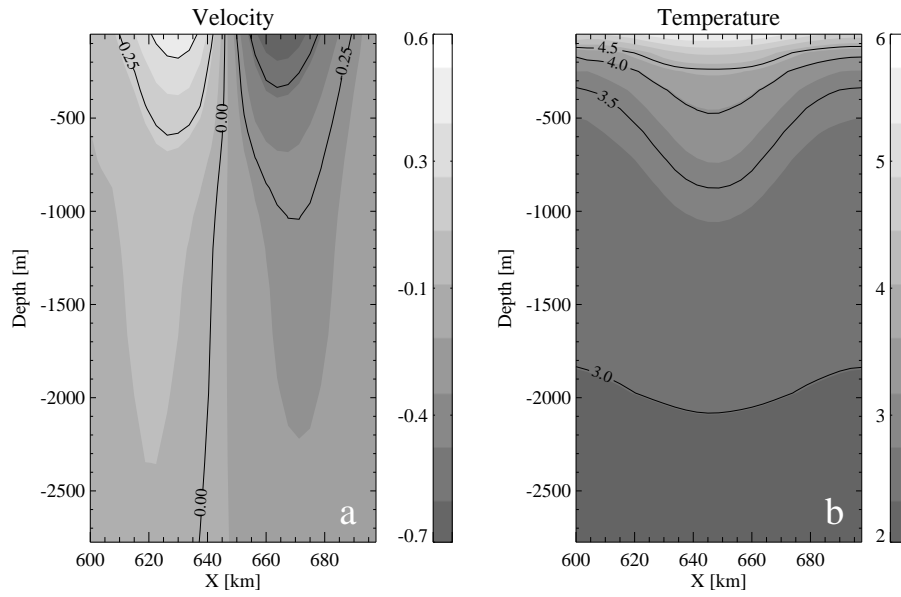


Figure 5: Zonal cross section of an example Irminger Ring from the model ( $y = 630$  km,  $t = 3$  months, see upper right panel of Figure 6). (a) Meridional velocity (contour interval is  $0.25 \text{ m s}^{-1}$ ). (b) Temperature (contour interval is  $0.5^\circ\text{C}$ ).

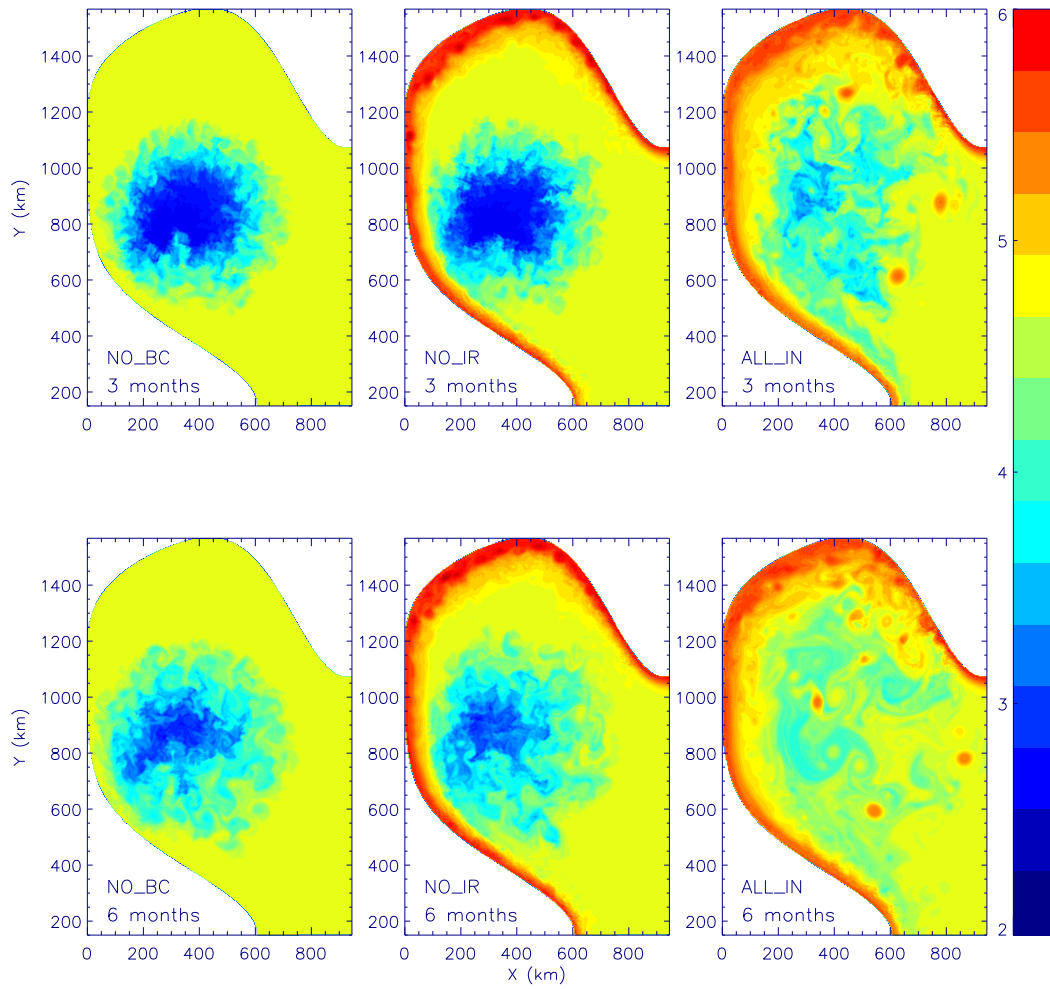


Figure 6: Snapshot of the surface temperature field ( $^{\circ}\text{C}$ ) for the three different cases. Left: *NO\_BC*. Middle: *NO\_IR*. Right: *ALL\_IN*. Upper row:  $t = 3$  months. Lower row:  $t = 6$  months.

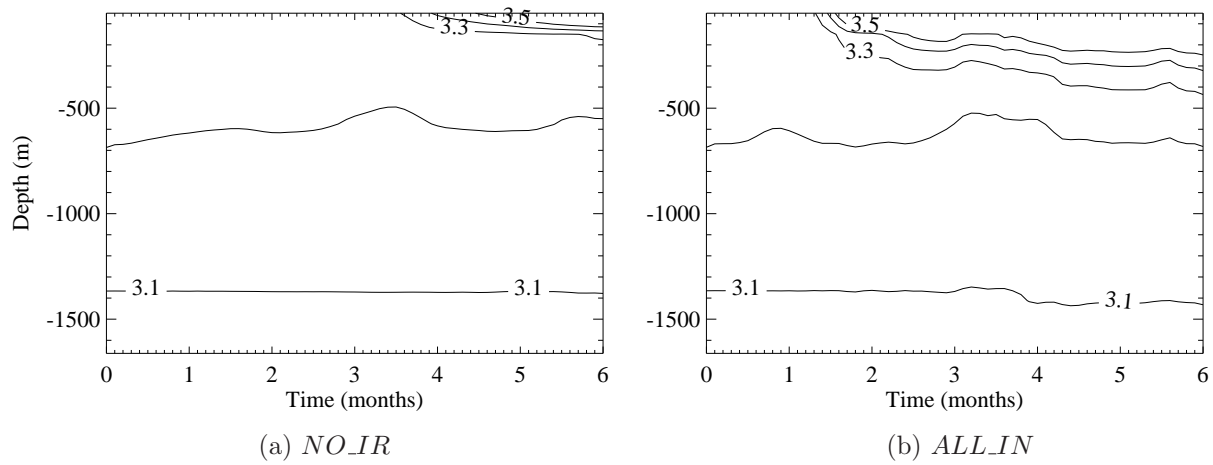


Figure 7: Time series of the temperature evolution averaged over an area in the center of the convection area ( $x = 350-450$  km,  $y = 825-925$  km) for the (a) *NO\_IR* case and the (b) *ALL\_IN* case. Contours are plotted every  $0.1^\circ\text{C}$ .

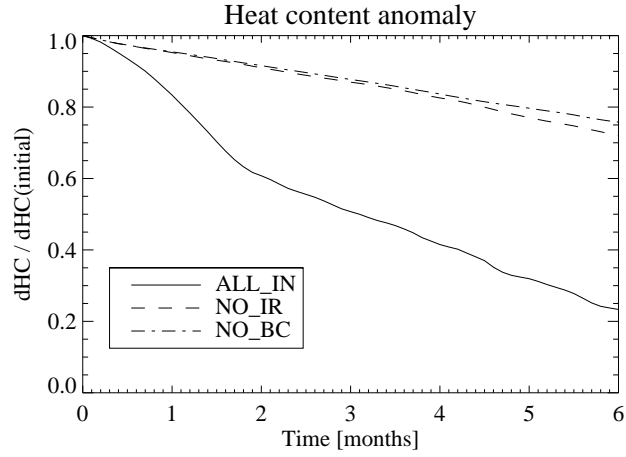


Figure 8: Heat content deficit of the convection area normalized by its initial value. The latter is defined as the reduction in the heat content that arises from the construction of the convection area (Section 2b). A zero heat content anomaly implies that the heat content of the convected cone has become exactly equal to the heat content of a cone before convection. Solid line: *ALL\_IN*. Dashed line: *NO\_IR*. Dash-dotted line: *NO\_BC*.

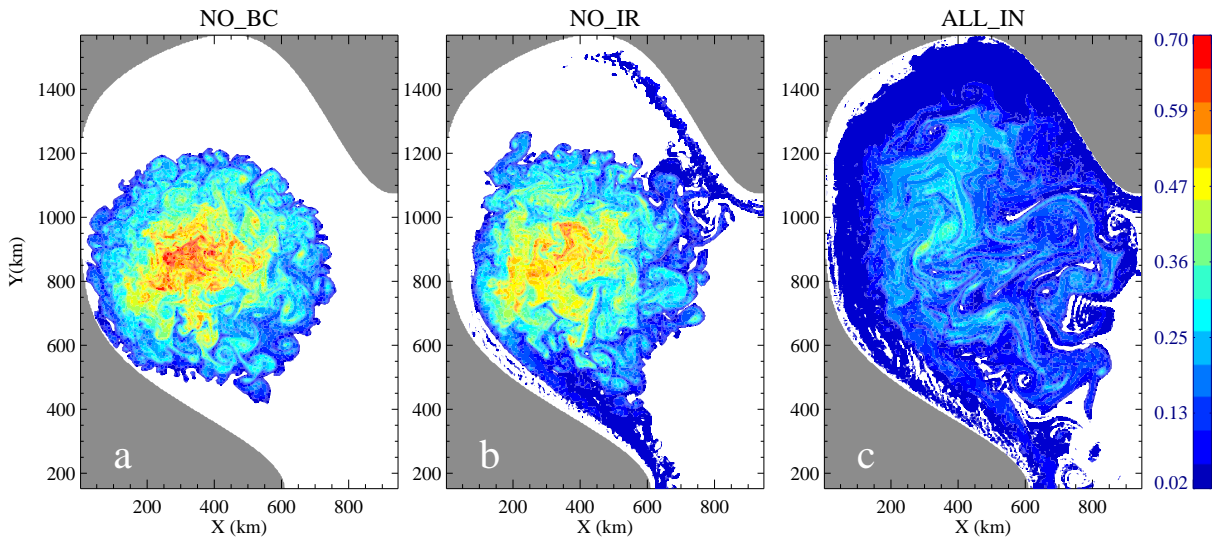


Figure 9: Depth-averaged concentration of a passive tracer after 6 months in the spindown simulations (a) *NO\_BC* (b) *NO\_IR* (c) *ALL\_IN*. The tracer was initialized to 1 inside the convected area and to 0 in the remainder of the domain.

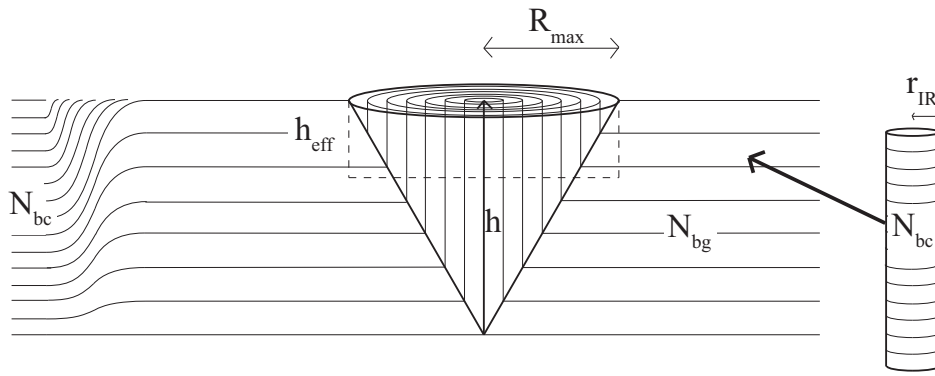


Figure 10: Definitions of the variables used in the derivations of the restratification time scales in Section 4a.

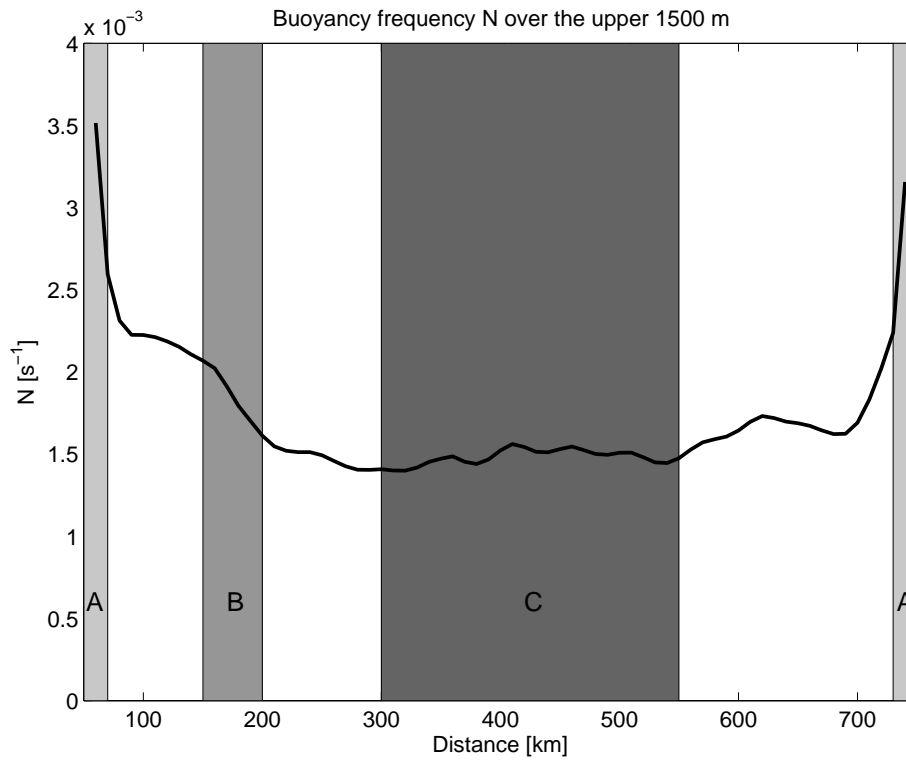


Figure 11: Buoyancy frequency averaged over the upper 1500 m of the water column from a mean late spring section over the 1990's (Pickart and Spall 2007). The shaded areas marked by A are used to determine  $N_{bc}$ , the area marked by B is used to determine  $N_{BCE}$ , and  $N_{bg}$  is found from the area marked by C.